A New Nitronyl-Nitroxide Ligand for Designing Binuclear Ln III Complexes: Syntheses, Crystal Structures, Magnetic and EPR Studies

Mihai Răducă, Daniel Martins, Cristian Spinu, Mihaela Hillebrand, Floriana Tuna, Gabriela Ionita, Augustin Mădălan, Constance Lecourt, Jean-pascal Sutter, Marius Andruh

▶ **To cite this version:**

Mihai Răducă, Daniel Martins, Cristian Spinu, Mihaela Hillebrand, Floriana Tuna, et al.. A New Nitronyl-Nitroxide Ligand for Designing Binuclear Ln III Complexes: Syntheses, Crystal Structures, Magnetic and EPR Studies. European Journal of Inorganic Chemistry, 2022, 2022 (16), pp.e202200128. 10.1002/ejic.202200128 . hal-03689254

HAL Id: hal-03689254
https://hal.science/hal-03689254

Submitted on 30 Jun 2022

HAL is a multi-disciplinary open access archive for the deposit and dissemination of scientific research documents, whether they are published or not. The documents may come from teaching and research institutions in France or abroad, or from public or private research centers.

L'archive ouverte pluridisciplinaire **HAL**, est destinée au dépôt et à la diffusion de documents scientifiques de niveau recherche, publiés ou non, émanant des établissements d'enseignement et de recherche français ou étrangers, des laboratoires publics ou privés.

A new nitronyl-nitroxide ligand for designing binuclear Ln^{III} complexes: syntheses, crystal structures, magnetic and EPR studies

Mihai Răducă,[a,b] Daniel O. T. A. Martins,[c] Cristian A. Spinu,[a,b] Mihaela Hillebrand,*[d] Floriana Tuna,*[c] Gabriela Ionita,[e] Augustin M. Mădălan,[a] Constance Lecourt,[f] Jean-Pascal Sutter,[f] Marius Andruh,*[a,b]

[a]*Inorganic Chemistry Department, Faculty of Chemistry, University of Bucharest, Regina Elisabeta Blvd. 4-12, Bucharest – 030018, Romania; E-mail: marius.andruh@acad.ro*
[b]*C. D. Nenitzescu Institute of Organic Chemistry of the Romanian Academy, Splaiul Independentei, 202B, 060023, Bucharest, Romania*
[c]*Department of Chemistry and Photon Science Institute, University of Manchester, Oxford Road, Manchester, M13 9PL, UK; Email: Floriana.Tuna@manchester.ac.uk*
[d]*Physical Chemistry Department, Faculty of Chemistry, University of Bucharest, Bucharest, Romania; Email: mihaela.hillebrand@gmail.com*
[e]*Ilie Murgulescu Institute of Physical Chemistry, Romanian Academy, Bucharest, Romania;*
[f]*Laboratoire de Chimie de Coordination du CNRS (LCC), Université de Toulouse, CNRS, Toulouse, France*

Abstract

A new nitronyl-nitroxid ligand (H_2L) featuring alcoholic and phenolic groups has been synthesised starting from 2-hydroxy-3-(hydroxymethyl)-5-methylbenzaldehyde (**A**). Using this ligand, three 2p-4f binuclear complexes have been obtained and crystallographically characterized: $[Ln_2(HL)_2(hfac)_4]$, (Ln = Gd **1**, Tb **2**, Dy **3**). Apart from the desired compounds, two by-products have been isolated as a molecular alloy containing an intermediate bearing hydroxylamino and N-oxide groups, i.e. (1-hydroxy-2-(2-hydroxy-3-(hydroxymethyl)-5-methylphenyl)-4,4,5,5-tetramethyl-4,5-dihydro-1H-imidazole 3-oxide, **B**, and the imino-nitroxide derivative, **C**. This system was characterized by single crystal X-ray diffraction, UV-VIS and EPR spectroscopy. During the synthesis of compounds **1**-**3**, two other complexes have been obtained and characterized: $[Ln(\mathbf{C})(hfac)_3]$ (**4**, Ln = Tb) and $[Ln_2(\mathbf{A}\text{-H})_2(hfac)_4]$ (**5**, Ln = Tb), where (**A**-H) results from the deprotonation of the phenolic group in **A**. The synthetic procedure was optimized in order to obtain pure **1** - **3** complexes. The cryomagnetic properties of compounds **1** - **3** have been investigated. Continuous-wave (CW) electron paramagnetic resonance (EPR) measurements were carried out at X- and Q-band for compound **1**. Time-dependent experiments were performed at three magnetic fields. Phase memory times, T_m, were found to be about 1000 ns at 6 K.

Introduction

Nitronyl-nitroxide ligands are exceptionally useful building-blocks for the controlled assembling of molecular magnetic materials.[1] Their magnetic exchange with 3*d* or 4*f* metal ions can vary from strongly antiferromagnetic to strongly ferromagnetic.[2] The coordination chemistry of these molecules is rather rich given the fact that they can act as both terminal and bridging ligands (in this last case through only one or both aminoxyl groups - Scheme 1). Moreover, the nitronyl-nitroxide platform can be decorated with additional coordinating groups, R, which can be neutral or anionic. The popularity of this family of ligands arises especially from the structural diversity provided by the R groups, that is, the number and the relative position of the donor atoms which can interact with metal ions. Discrete (oligonuclear) heterospin species and coordination polymers are thus assembled and show very interesting architectures and magnetic properties. It is worth mentioning that the presence of the two coordinating moieties (nitronyl-nitroxide and R groups) allows the synthesis of hetero-tri-spin complexes containing two different paramagnetic metal ions (for example, 2*p*-3*d*-4*f*).[3]

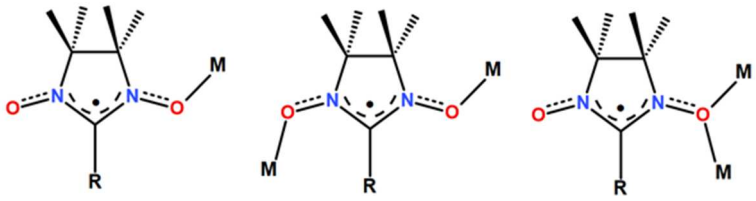

Scheme 1. Coordination modes of nitronyl-nitroxide ligands

Combination of the high versatility of the nitronyl-nitroxide ligands with the unique coordination properties of compartmental ligands [4] is an efficient strategy to form complexes with pre-established metal ion topologies. Recently, we demonstrated that an even better approach is to use bicompartmental ligands bearing a nitronyl-nitroxide fragment. In this design, the ligand compartment made by the Mannich-base moiety preferentially hosts the *3d* metal, while the compartment defined by the nitronyl–nitroxide pendant arm, comprising only oxygen atoms, will host the oxophilic lanthanide ion.[5] We have shown that strictly binuclear 2*p*-3*d*-4*f* heterospin complexes can be thus rationally assembled. Moreover, these ligands can be successfully used to obtain homo-binuclear 3*d* or mononuclear 4*f* complexes (the 3*d* metal ions do not have a particular preference for oxygen or nitrogen donor atoms, occupying the two compartments, while the Ln^{III} ions prefer the oxygen atoms).[5a] Following this reasoning, a nitronyl-nitroxide ditopic ligand with only oxygen donor atoms could lead to binuclear 2*p*-4*f*-4*f* complexes. In this paper we report on the chemistry generated by 2-hydroxy-3-

(hydroxymethyl)-5-methylbenzaldehyde, **A**, used as a precursor for a nitronyl-nitroxide ligand, H_2L (Scheme 2). The newly synthesized nitronyl-nitroxide acts as a bicompartmental ligand for lanthanide(III) ions. The crystal structures and magnetic properties, as well as the EPR spectra of the resulting binuclear complexes are discussed.

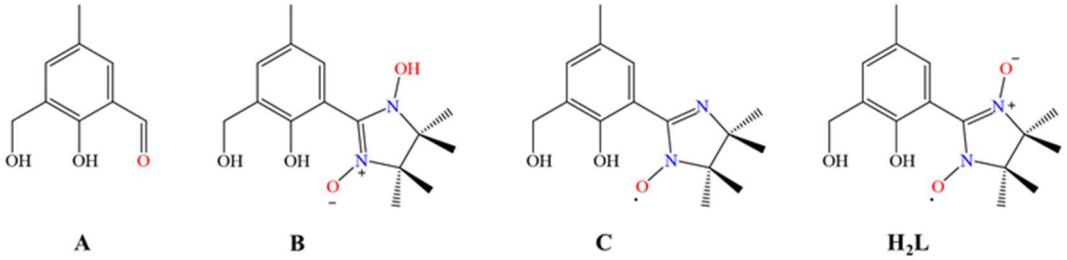

Scheme 2. Chemical structures of the organic molecules investigated in this paper

Results and discussion

Chemistry, crystal structures

2,6-Bis(hydroxymethyl)-*p*-cresol is a widely used precursor of bicompartmental ligands. It can be oxidized to the mono-aldehyde, **A** (Scheme 2), or to the dialdehyde, which further reacts with primary amines to produce compartmental Schiff-base ligands. On the other hand, the formyl group(s) can be transformed into nitronyl-nitroxide(s), following Ullman's synthetic protocol.[6] Let us focus first on the synthesis of the mono-radical, H_2L, starting from the monoaldehyde **A**. Compound **A** is reacted with 2,3-bis(hydroxylamino)-2,3-dimethylbutan, then oxidated with $NaIO_4$. Part of the mixture containing reagents and (by)products, to be further separated using column chromatography, was left for crystallization prior to separation. The obtained red single crystals have been analysed by single-crystal X-ray diffraction and were found to be a solid solution of two compounds (Figure 1): a compound featuring hydroxyl amino and N-oxide groups, **B**, and the imino-nitroxide, **C**. The two molecules are located on the same crystallographic positions, differing only by the presence or the absence of the OH

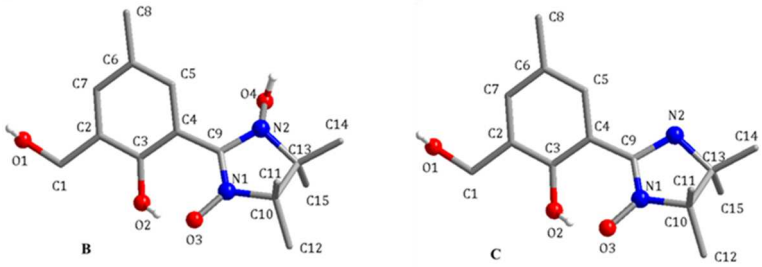

Figure 1. X-Ray structures of the two components in the solid solution of **B** and **C**. Part of hydrogen atoms was omitted for clarity.

group. The occupation factor for the oxygen atom of the hydroxyl amino group varies between 0.73 and 0.94 (for 9 different crystals arising from two different syntheses – see Table S1). While crystal structures of imino-nitroxides are common,[7] only one compound containing hydroxyl amino and N-oxide groups, similar to **B**, has been structurally characterized by X-Ray diffraction.[8] Selected bond distances and angles for **B** are provided in Table S2. The hydroxylamino nitrogen atom in **B** is chiral and the red molecular alloy (**B** + **C**) crystallizes in the $P2_12_12_1$ chiral space group. Each molecule is involved in H-bond interactions (Figure 2a), which generate supramolecular helicoidal chains (Figure 2b). The presence of the imino-nitroxide radical in the red molecular alloy (**B** + **C**) has been unambiguously proved by continuous-wave (CW) electron paramagnetic resonance (EPR) spectroscopy (Figure 3). An intense CW EPR signal has been observed for both solid state crystals and solution samples of the crystals dissolved in methanol. Interestingly, since the red crystals can be viewed as a diluted solid solution of the paramagnetic **C** in the diamagnetic **B**, the hyperfine structure of the EPR signal has been observed even in solid state (Figure 3a). The solution X-band EPR spectrum of component **C** from red crystals (**B** + **C**) dissolved in methanol displays a seven-line hyperfine structure due to coupling of the unpaired electron with the two inequivalent nitrogen nuclei of **C** (Figure 3b). Simulation of the EPR spectrum provided hyperfine constants of a_{N1} = 9.03 G and a_{N2} = 4.15 G, which are similar to those reported for imino-nitroxides.[9]

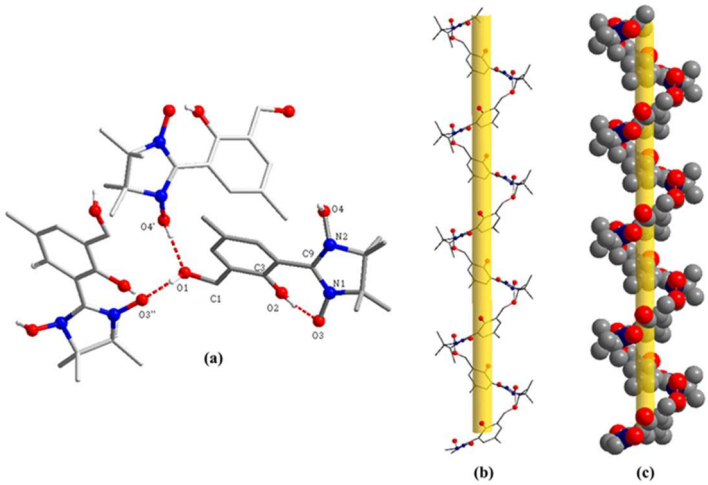

Figure 2. (a) Hydrogen bonds established between molecules **B** in the crystal, symmetry operations: ' = 1/2+x, 3/2-y, 1-z; '' = 1-x, 1/2+y, 1/2-z (part of hydrogen atoms was omitted for clarity). O2···O3 = 2.517 Å, O1···O3'' = 2.666 Å, O1···O4' = 2.644 Å; (b) perspective view of the supramolecular helicoidal chain (hydrogen atoms have been omitted for clarity); (c) space-filling perspective.

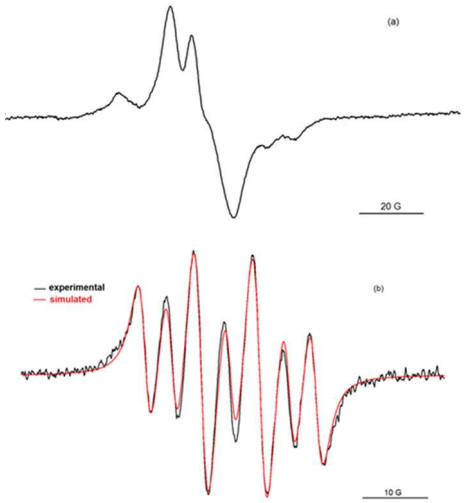

Figure 3. EPR spectra of **C** from the red crystals (**B**+**C**) in solid (a) and in MeOH (b). The hyperfine constants a_{N1} = 9.03 G and a_{N2} = 4.15 G.

The red colour of the crystals of the alloy (**B**+**C**) as well as of its methanolic solution is due to a band with a maximum at 570 nm (with a shoulder at ~ 610 nm) - Figure S1. The calculated electronic spectra of **B** and **C** in methanol show bands in the region 200-400 nm (Figure S2). Additionally, **C** is predicted to have a broader and weaker absorption at 560 nm, f=0.0051, assigned to a HOMO-LUMO transition of the β electrons (Figure S3); it corresponds to a transition from an orbital mainly localized on the phenyl to an orbital localized on the N-imino and NO groups. Therefore, we assume that the colour of the molecular alloy is due to the imino-nitroxide species (**C**).

After purification by column chromatography, the new ligand, H_2L, has been obtained and characterized (see experimental section). Trials to crystallize H_2L have not been successful. Subsequently, the ligand H_2L has been reacted with lanthanide(III) hexafluoroacetylacetonates (Gd^{III}, Tb^{III}, Dy^{III}). The inspection of the resulting crystalline materials under microscope revealed the presence of three different crystals: the desired compound, $[Ln_2(HL)_2(hfac)_4]$, (Ln = Gd **1**, Tb **2**, Dy **3**) and two by-products: $[Ln(\mathbf{C})(hfac)_3]$ (**4**, Ln = Tb) and $[Ln_2(\mathbf{A}\text{-}H)_2(hfac)_4]$ (**5**, Ln = Tb), where (**A**-H) results from the deprotonation of the phenolic group in **A** (Scheme 2). As expected, the X-ray powder diffraction measurements (PXRD) recorded for this crystalline material shows that the $[Ln_2(HL)_2(hfac)_4]$ phase is not pure (Figure S4). The crystal structures for the three $[Ln_2(HL)_2(hfac)_4]$ compounds, as well as for $[Tb(\mathbf{C})(hfac)_3]$ **4**, and $[Tb_2(\mathbf{A}\text{-}H)_2(hfac)_4]$ **5** have been solved (Figure 4). The synthesis has been further optimized in order to obtain the pure compounds **1** – **3**: the reactions between $[Ln(hfac)_3(H_2O)_2]$ and H_2L has been carried out in the presence of triethylamine. This procedure was successful, resulting in pure crystalline phases (the PXRD for compounds **1** – **3** are displayed in Figure S5). If an

excess of triethylamine is employed, a new white by-product crystallizes, $(Et_3NH)[Tb(hfac)_4]$ **6** (Figure S6).

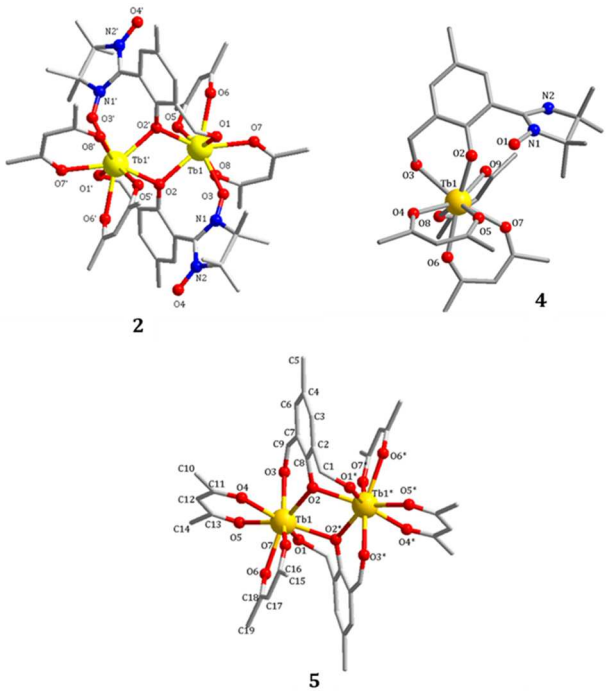

Figure 4. Perspective views of the molecular structures of **2** (symmetry operations: ' = -x, 1-y, -z), **4** and **5** (symmetry operations: * = 1-x, 1-y, 1-z). Hydrogen and fluorine atoms have been omitted for clarity.

Let us come back to the crystal structures displayed in Figure 4. Compounds **1** – **3** are isostructural and only the crystal structure of the terbium derivative is described here. It consists of centrosymmetric binuclear units (Figure 4a), the terbium ions being bridged by the phenoxido groups arising from two single deprotonated radicals, HL^-. Each terbium ion shows a coordination number of 8, with a square antiprism stereochemistry (the SHAPE[10] parameters for compounds **1** – **3** are presented in Table S3). The coordination sphere is made by 8 oxygen atoms arising from two chelating $hfac^-$ ligands, one aminoxyl oxygen, one alcoholic OH group, and two phenoxido bridging oxygens, with distances varying between 2.343(4) and 2.407(4) Å. The intramolecular distance between the Tb^{III} ions is 3.9063(5) Å. In the case of the imino-nitroxide derivative **4** (Figure 4b), the lanthanide ion is coordinated by six oxygen atoms from three chelating $hfac^-$ ligands, one phenolic and one alcoholic oxygen atoms, with a triangular dodecahedron stereochemistry. The metal–oxygen distances vary between 2.293(5) and 2.416(5) Å. The aminoxyl group is not coordinated. The crystal structure of **5** (Figure 4c) is similar to the one of **2**, consisting in centrosymmetric bis(phenoxido)-bridged units, with a carbonyl oxygen atom instead of the aminoxyl oxygen atom, and octa-coordinated lanthanide ions, with a triangular dodecahedron stereochemistry. The metal-oxygen distances vary

between 2.298(3) and 2.419(4) Å. The intramolecular distance between the Tb ions is 3.8254(5) Å. The SHAPE parameters for **4** and **5** are presented in Table S4. Selected bond distances and angles for compounds **1** – **3** are collected in Table S5, and Table S6 (for **4** and **5**).

Magnetic properties and EPR spectra

The $\chi_M T$ vs. T and M vs H behaviours (χ_M stands for the molar magnetic susceptibility) for compounds **1** – **3** are shown in Figure 5 and Figure S7, respectively. The $\chi_M T$ value at 300 K is 16.8 $cm^3mol^{-1}K$ for **1**, 24.1 $cm^3mol^{-1}K$ for **2**, and 28.9 $cm^3mol^{-1}K$ for **3**, in good agreement with those expected for the paramagnetic contributions of the metal ions (Gd^{III}, $S = 7/2$; Tb^{III}, $J = 6$, $g_J = 3/2$; Dy^{III}, $J = 15/2$, $g_J = 4/3$) and two S = ½ radicals in the absence of exchange interactions (*i.e.* **1**: 16.51; **2**: 24.39; **3**: 29.09 $cm^3mol^{-1}K$). For **1**, $\chi_M T$ remains constant between 300 and 80 K, when it starts to decrease reaching 10.5 $cm^3mol^{-1}K$ at 2 K. This behaviour can be ascribed to overall antiferromagnetic interactions arising from the interplay of two exchange pathways, namely the Gd^{III}-Gd^{III} exchange interaction mediated by the two phenoxido bridges, and the Gd^{III}-Rad interactions. The first one was found to be weak and antiferromagnetic in numerous compounds.[11] On the other hand, the Gd^{III}-nitronyl-nitroxide exchange interactions were found both ferro- and antiferromagnetic,[11c,12] and are strongly influenced by the Gd-O-N and Gd-O-N-C angles, as well as the Gd–O distance.[13] According to recent magneto-structural correlations supported by theoretical calculations,[13] these geometrical parameters for **1** (Gd-O-N = 139.6(7)º Gd-O-N-C = 52.3(17)º, Gd–O = 2.365(8) Å) suggest a likely ferromagnetic Gd^{III}-Rad interaction; obviously in the present complex the behaviour is overwhelmed by the antiferromagnetic Gd^{III}-Gd^{III} interaction. The featureless variation of $\chi_M T$ with the temperature

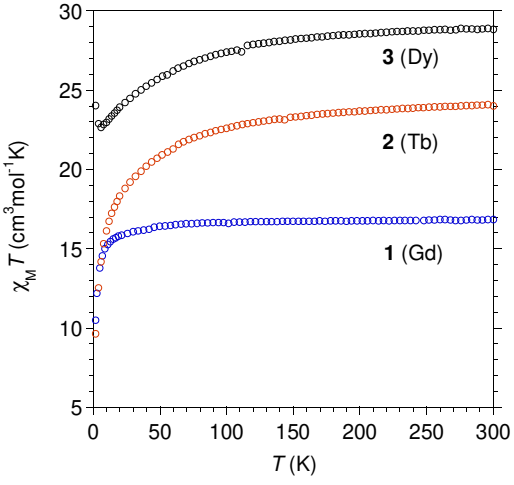

Figure 5. Temperature dependence the $\chi_M T$ product for **1**, **2**, and **3**.

does not allow the determination of the magnetic exchange parameters. The dominant antiferromagnetic contribution in **1** is also supported by the field dependence of the magnetization recorded at 2 K (Figure S7). In the low field range, the experimental behaviour runs below the behaviour calculated with the Brillouin functions for non-interacting $S = 7/2$ and $S = ½$ spins.

For **2**, a slow decrease of $\chi_M T$ is observed from 300 K and becomes more pronounced while the temperature is lowered, to reach 9.6 $cm^3mol^{-1}K$ at 2 K. This behaviour is characteristic of the crystal field effects associated with Tb^{III} ions, combined with the intramolecular exchange interactions at low temperature. The overall behaviour for the dysprosium derivative, **3**, is similar to that of **2** except the up-turn exhibited by $\chi_M T$ below 7 K (22.7 $cm^3mol^{-1}K$) to reach 24.0 $cm^3mol^{-1}K$ at 2 K. This behaviour suggests that the antiferromagnetic contribution is smaller with Dy, allowing the ferromagnetic Dy-Rad interactions to dominate.

The ac magnetic susceptibility measurements in zero-field and with applied DC field did not reveal an out-of-phase susceptibility component, thus excluding any slow relaxation of the magnetization for compounds **2** and **3**.

CW EPR studies conducted on powder samples of **1** have shown significant broadening of the EPR signal upon cooling from room temperature to 10 K (Figure 6), indicative of small Gd-Gd and/or Gd-radical interactions. However, the strength of these interactions cannot be accurately determined given the spectra are broad and retain the dominant features of the individual Gd^{III} ion ($S = 7/2$, $I = 0$ nuclei counting for 70% natural abundance). Even at room temperature where no magnetic exchange is expected to occur between paramagnetic components, CW EPR

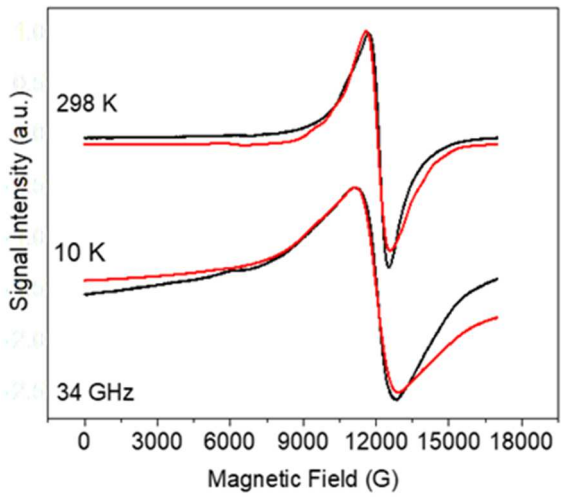

Figure 6. Experimental (black) and simulated (red) powder EPR spectra at Q-band (34 GHz) for **1** at 10 and 298 K. See text for simulation parameters.

spectra of powder samples of **1** show no evidence of nitronyl-nitroxide spectral features and thus can be reasonably modelled with the spin Hamiltonian in eq. (1), which includes the electron Zeeman (EZ) interaction and the zero-field splitting (ZFS) interaction, where the coefficients D and E are the axial and rhombic ZFC parameters, respectively, and g is the electron spin g-factor. This is because the spectral lines of organic radicals are much narrower and possibly masked by the broad features of multi-electron Gd^{III} ions.

$$H = \beta BgS + D[S_z^2 - (1/3)S(S+1)] + E(S_x^2 - S_y^2) \qquad (1)$$

Reasonably good fits were obtained with $g = 1.996$, $D = 0.04$ cm^{-1} and $|E| = 0.013$ cm^{-1} for both X- and Q-band frequencies. Interestingly, the same parameters reproduce the low temperature data (Figure 6 and Figure 7), as well as the frozen solution spectra, thought the later show an additional sharp line due to the nitronyl-nitroxide radicals in **1** (Figure S8). The fact that the orthorombicity $|E|/D$ is close to the maximum value (1/3) may reflect the low symmetry of the coordination sphere of Gd^{III}. Since Gd-Gd molecular dimers were proposed as attractive building blocks for quantum computation,[14] due to the abundance of electronuclear states, we attempted to investigate the ability of **1** as a possible hybrid platform incorporating both a Gd-Gd dimer and radical ions. Figure 8 shows a well resolved echo-detected field swept (EDFS) spectrum for **1**, measured from a 1.2 mM toluene:methanol solution at 6 K, using a primary Hahn echo mw pulse sequence.[15] Time-dependent experiments were performed at three magnetic fields marked by the observer positions (OP1-3): 3280 G (OP1), 3504 G (OP2) and 3570 G (OP3). OP1 and OP3 are resonance fields corresponding to the Gd^{III} ion, while OP2 is mainly attributed to the nitronyl-nitroxide radical. Phase memory times, T_m, were found to be

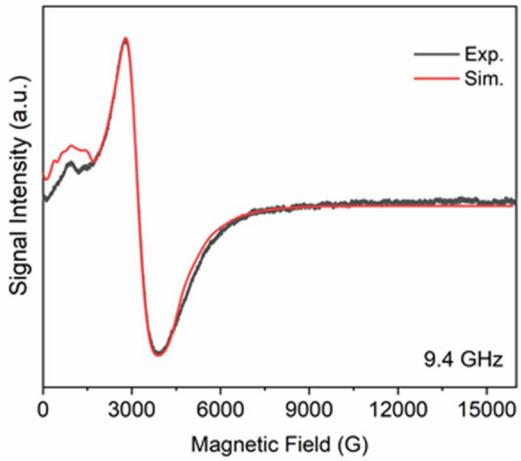

Figure 7. Powder EPR spectrum for **1** at X-band (9.4 GHz) and 30 K (black) and its simulated version (red) with the parameters in the text.

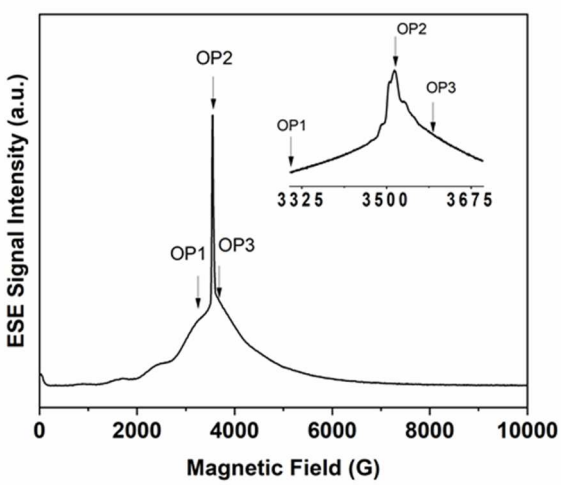

Figure 8. X-band (9.7 GHz) EDFS spectrum of 1.2 mM solution (methanol:toluene, 9:1 v/v) of **1** at 6 K. The arrows mark the field observer positions where time-dependent experiments were performed.

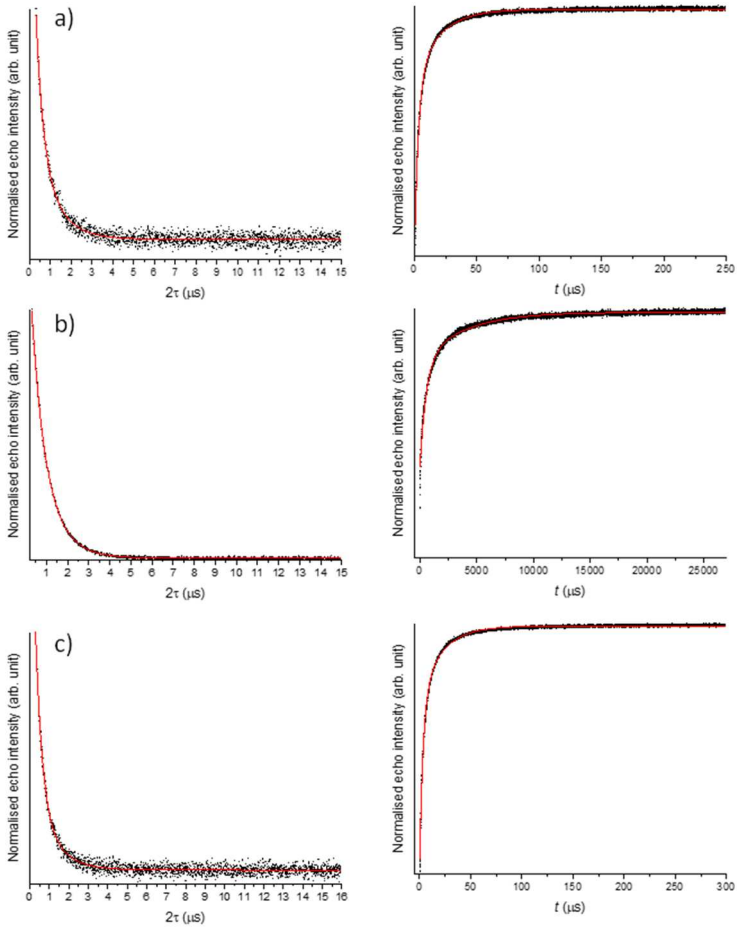

Figure 9. (Left) Normalised Hahn echo intensities as a function of the interpulse delay 2, and (right) inversion recovery data as a function of the interpulse delay *t* (right), for a 1.2 mM methanol / toluene 9:1 (v/v) solution at 6 K and different observer positions: (a) 3280 G (OP1); (b) 3504 G (OP2) and (c) 3570 G (OP3) (black scatter). The red lines represent the best fits to the biexponential equation (**2**).

about 1000 ns at 6 K regardless of the magnetic field position. In contrast, the spin-lattice relaxation time, T_1, is considerably longer (ca. 3.7 ms) at the radical position (OP2) compared to the isolated Gd^{III} ion (19.3 µs at OP1; 20.77 µs at OP3) (Figure 9 and Table 1).

Table 1. Extracted relaxation times from the experimental data presented in Figure 9.

Magnetic Field (G)	T_m (ns)	T_1 (ns)	T_{SD} (ns)
3280 (OP1)	1021 (70)	19,330 (92)	3182 (16)
3504 (OP2)	1140 (52)	3,735,886 (26,604)	543,920 (4,070)
3570 (OP3)	1079 (74)	20,770 (77)	3434 (14)

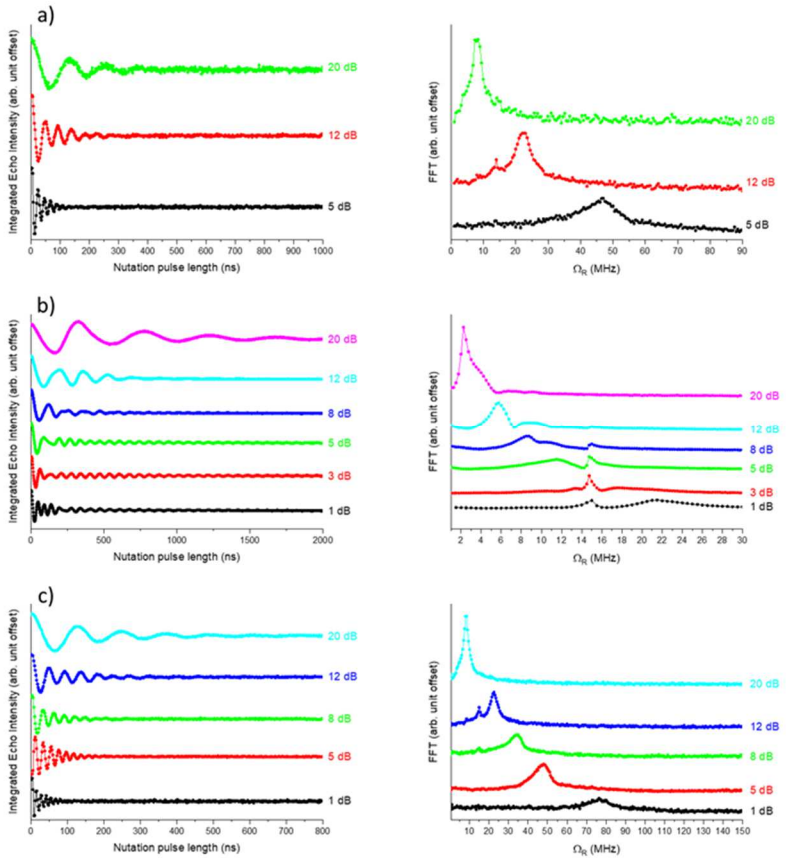

Figure 10. Rabi oscillations acquired with different microwave attenuations (left) and corresponding Fourier transforms (right) for a 1.2 mM methanol / toluene 9:1 (v/v) solution of **1** at 6 K (a) 3280G (OP1), (b) 3504 G (OP2) and (c) 3570 G (OP3). Solid lines are guide to the eye. The peak at around 15 MHz corresponds to the Larmor frequency of ^{1}H nucleus.

The observed phase memory times were long enough to perform transient nutation experiments to probe whether the spin states of **1** can be coherently manipulated and placed at an arbitrary position within the Bloch sphere. Rabi oscillations were detected at all observer positions (Figure 10) and with variable microwave attenuation (from 0 to 20 dB). It was observed that

the Rabi frequency of such oscillations varies linearly with the microwave power B_1 (Figure), however the Rabi frequency at 3504 mT (OP2) follows a different trend from the other fields, confirming that this observer position does indeed refers to a different electronic spin.

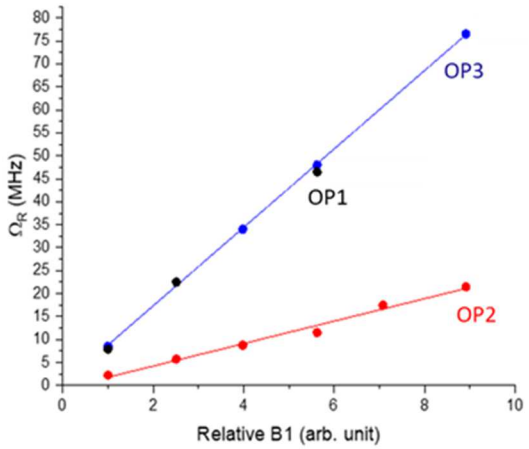

Figure 11. Relative B1 dependence of the Rabi frequency, Ω_R, for a 1.2 mM methanol / toluene 9:1 (v/v) solution of 1 at 6 K and different observer positions. Blue and red lines emphasise the linear dependence on B1.

Conclusions

A new two-pocket nitronyl-nitroxide ligand and its binuclear lanthanide complexes have been successfully synthesised and structurally characterized. In this paper we also have shown that the careful investigation of all products resulted during the preparation of nitronyl-nitroxides and their lanthanide coordination compounds provide useful information about the complexity of these reactions. The case of the molecular alloy containing an imino-nitroxide and a rarely characterized compound containing hydroxylamino and N-oxide groups is particularly interesting. The EPR spectra of the gadolinium derivative, **1**, have been investigated at X- and Q-band. Time-dependent experiments were performed at three magnetic fields and Rabi oscillations have been detected. Phase memory times, T_m, were found to be about 1000 ns at 6 K.

Experimental Section

Materials and Methods

All starting materials were of reagent grade and used without purification. Syntheses of 2,3-dimethyl-2,3-dinitrobutane[16] and 2-hydroxy-3-(hydroxymethyl)-5-methylbenzaldehyde[17] and rare-earth trishexafluoroacetylacetonato[18] compounds were performed following the reported procedures. The synthesis of the precursor 2,3-bis(hydroxylamino)-2,3-dimethylbutan was performed according to the previously reported procedure.[19]

The synthesis of ligand H_2L was devised and adapted from reported procedures.[6,20]

To a solution of 2,3-dimethyl-2,3-dinitrobutane (0.3005 g, 2.0275 mmol) in 40 mL MeOH was added 2-hydroxy-3-(hydroxymethyl)-5-methylbenzaldehyde (0.3063 g, 1.8431 mmol). The mixture was refluxed for 1 h followed by evaporation of the solvent under vacuum. The yellow intermediate was dissolved in 40 mL $CHCl_3$ and was cooled on ice bath. Then under vigorous stirring $NaIO_4$ (0.3866 g, 1.8074 mmol) was added followed by 40 mL of water. The biphasic system was vigorously stirred, and the reaction was left to evolve at 0°C for 15 min. The organic phase was isolated using a separatory funnel and dried with $MgSO_4$. The solvent was evaporated under vacuum to obtain the crude blue product which was purified using column chromatography with diethyl ether. Best yield: 31%. The red crystals (**B+C**) were obtained from a methanolic solution by slow evaporation of the solvent prior to column chromatography. Selected IR data (ATR, cm^{-1}): 3462(bw), 2990(m), 2917(m), 2864(m), 1679(m), 1598(m), 1523(w), 1451(vs), 1379(s), 1329(vs), 1250(m), 1209(m), 1149(s), 1056(m), 1017(m), 865(w), 794(w), 671(w), 547(w), 448(w). ^{1}H-NMR (500.13 MHz, MeOD-d_4, δ ppm): 7.41 (s, 2H, Ar***H***), 4.69 (s, 2H, C***H***$_2$), 2.32 (s, 3H, Ph-C***H***$_3$), 1.35 (s, 12H, C***H***$_3$). N.B. To measure the NMR spectrum of H_2L, it was reduced with phenylhydrazine and hydrazine to obtain information in aliphatic and aromatic region, respectively. MS (exact mass 293.15), +ESI: 293.0, -ESI: 292.7. For EPR spectrum see Figure S9.

$[Gd_2(HL)_2(hfac)_4]$ (**1**).

$Gd(hfac)_3{\cdot}2H_2O$ (0.0278 g, 0.0341 mmol) was dissolved in 15 mL of *n*-heptane and boiled under stirring until a third of the solvent has been evaporated. A solution of H_2L (0.0100 g, 0.0341 mmol) in 3 mL of $CHCl_3$ was added followed by a drop triethylamine. The mixture was

stirred for one minute and then the vial was sealed. After one day a microcrystalline blue powder has been obtained.
Yield: 63%. IR data (KBr, cm^{-1}): 1660(m), 1533(w), 1513(m), 1468(w), 1353(m), 1258(s), 1202(s), 1146(vs), 799(w), 661(w), 589(w). Elemental analysis: calcd (%) for $C_{50}H_{44}N_4O_{16}F_{24}Gd_2$: C, 34.77; H, 2.57; N, 3.24; found (%): C, 35.21; H, 2.99; N, 3.29.

$[Tb_2(HL)_2(hfac)_4]$ (**2**) has been prepared following the same procedure described for (**1**) using $Tb(hfac)_3 \cdot 2H_2O$ (0.0278 g, 0.0341 mmol).
Yield: 69%. IR data (KBr, cm^{-1}): 1660(m), 1533(w), 1513(m), 1468(w), 1353(m), 1258(s), 1202(s), 1146(vs), 799(w), 661(w), 589(w). Elemental analysis: calcd (%) for $C_{50}H_{44}N_4O_{16}F_{24}Tb_2$: C, 37.70; H, 2.56; N, 3.23; found (%): C, 34.64; H, 2.96; N, 2.96.

$[Dy_2(HL)_2(hfac)_4]$ (**3**) has been prepared following the same procedure described for (**1**) using $Dy(hfac)_3 \cdot 2H_2O$ (0.0279 g, 0.0341 mmol)
Yield: 65%. IR data (KBr, cm^{-1}): 1660(m), 1533(w), 1513(m), 1468(w), 1353(m), 1258(s), 1202(s), 1146(vs), 799(w), 661(w), 589(w). Elemental analysis: calcd (%) for $C_{50}H_{44}N_4O_{16}F_{24}Dy_2$: C, 34.56; H, 2.55; N, 3.22; found (%): C, 34.62; H, 2.94; N, 3.07.

Physical Measurements

IR spectra were recorded on a FTIR Bruker Tensor V-37 spectrophotometer (KBr pellets) in the range of 4000–400 cm^{-1} and on a FTIR Bruker Vertex 70 spectrometer in the 4500–400 cm^{-1} range using the ATR technique. UV–Vis diffuse reflectance spectra were recorded on a JASCO V-670 spectrophotometer on undiluted samples from 200 to 1000 nm. The absorption spectra were recorded with a JASCO V-630 spectrophotometer. Elemental analyses (C, H, N) were performed on a EuroEa Elemental Analyzer.

Magnetic Measurements

Magnetic studies for all the samples were carried out with a Quantum Design MPMS 5S SQUID magnetometer in the temperature range 2–300 K. The measurements were performed on polycrystalline samples mixed with grease and put in gelatin capsules. The temperature dependences of the magnetization were measured in an applied field of 0.1 T and the isothermal field dependence of the magnetizations were collected up to 5 T. Explerimental molar susceptibility (χ_M) values were corrected for the diamagnetic contribution of the sample holder and grease, by measurement, and of the atoms in the molecules, by using Pascal's tables. Slow

relaxation of the magnetization was examined through AC susceptibility measurements under zero and applied dc fields.

Continuous-wave (CW) electron paramagnetic resonance (EPR) measurements were carried out at X- (~9.5 GHz) or Q-band (~34 GHz) with either a Bruker EMX Micro or a Bruker EMX Plus EPR Spectrometer operating at variable temperatures. The magnetic field values were corrected against the Bruker strong pitch standard (g = 2.0028). Pulse experiments were done on a Bruker E580 spectrometer operating at X-band band (*ca.* 9.7 GHz). Echo-detected field swept (EDFS) spectra were collected using a two-pulse Hahn-echo sequence ($\pi/2 - \tau - \pi - \tau -$ echo) at fixed interpulse delay time and varying the static magnetic field. Pulse measurements were performed on solution samples (1.2 mM in methanol: toluene 9:1 (v/v)) at 6 K.

Cryogenic temperatures were achieved using a cryogen-free closed-cycle helium circuit and the EasySpin software was used to simulate the spectra.[21]

Phase memory times were measured using a Hahn echo sequence and varying the interpulse delay 2τ at a fixed magnetic field. Long pulses of 64 ns were necessary to suppress modulation effects from proton and nitrogen-14 nuclei. The curves were fitted with the biexponential equation (**2**),

$$Y(t) = Y_{0,f} \exp\left(-\frac{t}{T_{m,f}}\right) + Y_{0,s}\exp(-\frac{t}{T_{m,s}}) \qquad (2)$$

where the subscripts f and s stand for fast and slow respectively, $Y_{0,\mathrm{f}}$ and $Y_{0,s}$ measure the amplitudes of the fast and slow relaxation processes, respectively, while T_m is the memory time. The fast T_m component can be attributed to some molecules that have spin-spin interaction with neighbours, which may occur in randomly diluted systems.[22]

Spin-lattice relaxation time, T_1, was measured with an inversion recovery mw pulse sequence ($\pi - t - \pi/2 - \tau - \pi - \tau -$ echo) by varying the interpulse delay t at a fixed τ. The resulted magnetisation recovery curves were fitted with a biexponential equation similar to eq. (**2**), where the fast component is associated with spectral diffusion, commonly one order of magnitude smaller than T_1.

Rabi oscillations were detected using a transient nutation pulse sequence ($t_\mathrm{p} - t - \pi/2 - \tau - \pi - \tau -$ echo) and varying the tipping pulse length. The oscillations curves were baselined using a polynomial function and the Rabi frequency, Ω_R, was determined by applying a Fourier Transform to the recorded time-dependent data.

Computational Details

The calculation were performed with the Gaussian 09 Program[23] considering **the geometries optimized in methanol** , the uB3LYP[24] functional and the TZVP[25] basis set. **Am scos fosta trimitere 25 si am renumerotat**!!

X-ray Crystallography

X-ray diffraction measurements for the all crystals were performed on a Rigaku XtaLAB Synergy-S diffractometer operating with Mo-Kα (λ = 0.71073 Å) micro-focus sealed X-ray tube. The structures were solved by direct methods and refined by full-matrix least squares techniques based on F^2. The non-H atoms were refined with anisotropic displacement parameters. Calculations were performed using SHELX-2014 or SHELX-2018 crystallographic software package. The X-ray powder diffraction measurements (PXRD) were carried out on a Proto AXRD Benchtop using the Cu-Kα radiation with a wavelength of 1.54059 Å in the range 5-35º 2θ. Data collection and refinement parameters for compounds **1-3** are summarized in Table 2 and in Table S7 for compounds **4-6**, respectively.

Table 2. Crystallographic data and structure refinement for **1-3**.

Compound	**1**	**2**	**3**
Chemical formula	$C_{50}H_{44}F_{24}Gd_2N_4O_{16}$	$C_{50}H_{44}F_{24}Tb_2N_4O_{16}$	$C_{50}H_{44}F_{24}Dy_2N_4O_{16}$
M (g mol^{-1})	1727.39	1730.73	1737.89
Temperature, (K)	293(2)	293(2)	293(2)
Wavelength, (Å)	0.71073	0.71073	0.71073
Crystal system	*Monoclinic*	*Monoclinic*	*Monoclinic*
Space group	*P21/n*	*P21/n*	*P21/n*
a (Å)	13.8299(7)	13.8055(5)	13.7174(9)
b (Å)	16.1240(6)	16.1049(5)	16.0695(7)
c (Å)	15.5856(6)	15.5746(5)	15.5249(8)
α (º)	90	90	90
β (º)	110.977(5)	110.602(4)	109.692(6)
γ (º)	90	90	90
V (Å^3)	3245.1(3)	3241.3(2)	3222.0(3)
Z	2	2	2
D_c (g cm^{-3})	1.768	1.773	1.791
μ (mm^{-1})	2.159	2.298	2.436
F(000)	1688	1692	6961
Goodness-of-fit on F^2	1.140	1.028	1.114
Final R_1, wR_2 [I>2σ(I)]	0.0692, 0.1811	0.0392, 0.1031	0.0670, 0.1426
R_1, wR_2 (all data)	0.0881, 0.1976	0.0497, 0.1092	0.0927, 0.1535
Largest difference peak and hole (e Å^{-3})	1.777, -1.094	1.099, -0.521	1.376, -0.595

CCDC 2153407 (for **B1**), 2153408 (for **B2**), 2153409 (for **B3**), 2153410 (for **B4**), 2153411 (for **B5**), 2153412 (for **B6**), 2153413 (for **B7**), 2153414 (for **B8**), 2153415 (for **B9**), 2153416 (for **1**), 2153417 (for **3**), 2153418 (for **2**), 2153419 (for **5**), 2153420 (for **6**), 2153421 (for **4**) contain the supplementary crystallographic data for this paper. These data can be obtained free of charge from The Cambridge Crystallographic Data Centre.

Conflicts of interest

There are no conflicts to declare.

Acknowledgements

Financing from UEFISCDI (Project PN-III-P4-ID-PCCF-2016-0088, 1/2018) is gratefully acknowledged. MR is thankful to Sergiu Calancea for the organic synthesis as well as to Anamaria Hanganu for NMR, Maria Maganu for FTIR-ATR and Victorița Tecuceanu for MS measurements. D.O.T.A.M. thanks the University of Manchester for a Presidential Doctoral Scholarship. We also thank the EPSRC UK National EPR Facility at Manchester for support with EPR measurements (NS/A000055/1).

Keywords

Lanthanides, binuclear complexes, nitronyl-nitroxide, magnetism, EPR

REFERENCES

1. a) D. Luneau, *Eur. J. Inorg. Chem*. **2020**, 597; b) S. Demir, I.-R. Jeon, J. R. Long, T. D. Harris, *Coord. Chem. Rev*. **2015**, *289-290*, 149; c) X. Meng, W. Shi, P. Cheng, *Coord. Chem. Rev*. **2019**, *378*, 134; d) M. T. Lemaire, *Pure Appl. Chem*. **2004**, *76*, 277; e) C. Benelli, D. Gatteschi, *Chem. Rev*. **2002**, *102*, 2369; f) D. Luneau, P. Rey, *Coord. Chem. Rev.* **2005**, *249*, 2591; g) A. Caneschi, D. Gatteschi, R. Sessoli, P. Rey, *Acc. Chem. Res.* **1989**, *22*, 392.
2. See, for example: a) T. Nakamura, T. Kanetomo, T. Ishida, *Inorg. Chem*. **2021**, *60*, 535; b) T. Kanetomo, T. Yoshitake, T. Ishida, *Inorg. Chem*., **2016**, *55*, 8140; c) M. Perfetti, A. Caneschi, T. S. Sukhikh, *Inorg. Chem*., **2020**, *59*, 16591.
3. See, for example: a) L. B. L. Escobar, G. P. Guedes, S. Soriano, N. L. Speziali, A. K. Jordão, A. C. Cunha, V. F. Ferreira, C. Maxim, M. A. Novak, M. Andruh, M. G. F. Vaz, *Inorg. Chem*. **2014**, *53*, 7508; b) M. Zhu, L. Li, J.-P. Sutter, *Inorg. Chem. Front*. **2016**, *3*, 994; c) L. Xi, J. Suan, K. Wang, J. Lu, P. Jing, L. Li, *Dalton Trans*. **2020**, *49*, 1089; d) G. Novitchi, S. Shova, Y. Lan, W. Wernsdorfer, C. Train, *Inorg. Chem.* **2016**, *55*, 12122; e) M. G. F. Vaz, M. Andruh, *Coord. Chem. Rev.* **2021**, *427*, 213611; f) M. Briganti, F. Totti, M. Andruh, *Dalton Trans*., **2021**, *50*, 15961.
4. See, for example: a) P. A. Vigato, S. Tamburini, *Coord. Chem. Rev*., **2008**, *252*, 1871; b) P. A. Vigato, S. Tamburini, *Coord. Chem. Rev*., **2004**, *248*, 1717.
5. a) A. A. Patrascu, S. Calancea, M. Briganti, S. Soriano, A. M. Madalan, R. A. A. Cassaro, A. Caneschi, F. Totti, M. G. F. Vaz, M. Andruh, *Chem. Commun*. **2017**, *53*, 6504; b) A. A. Patrascu, M. Briganti, S. Soriano, S. Calancea, R. A. A. Cassaro, F. Totti, M. G. F. Vaz, M. Andruh, *Inorg. Chem*. **2019**, *58*, 13090.
6. a) J. H. Osiecki, E. F. Ullman, *J. Am. Chem. Soc*. **1968**, *90*, 1078; b) E. F. Ullman, L. Call, J. H. Osiecki, *J. Org. Chem*. **1970**; *35*, 3623; c) E. F. Ullman, J. H. Osiecki, D. G. B. Boocock, R. Darcy, *J. Am. Chem. Soc*. **1972**, *94*, 7049; d) C. Hirel, K. E. Vostrikova, J. Pécaut, V. I. Ovcharenko, P. Rey, *Chem. Eur. J*. **2001**, *7*, 2007.
7. See, for example: a) H. Oshio, T. Ito, *Coord. Chem. Rev*. **2000,** *198*, 329; b) V. I. Ovcharenko, O. V. Kuznetsova, *Russ. J. Coord. Chem*. **2020**, *89*, 1261.
8. E. V. Tretyakov, I. V. Eltsov, S. V. Fokin, Y. G. Shvedenkov, G. V. Romanenko V. I. Ovcharenko, *Polyhedron*, **2003**, *22*, 2499.
9. See, for example: a) T. Akita, Y. Mazaki, K. Kobayashi, *J. Org. Chem.* **1995**, *60*, 2092; b) E. Onal, Y. Yerli, B. Cosut, G. Pilet, V. Ahsen, D. Luneau, C. Hirel, *New J. Chem*. **2014**, *38*, 4440.
10. a) D. Casanova, J. Cirera, M. Llunell, P. Alemany, D. Avnir, S. Alvarez, *J. Am. Chem. Soc.* **2004**, *126*, 1755; b) D. Casanova, M. Llunell, P. Alemany, S. Alvarez, *Chem. Eur. J.* **2005**, *11*, 1479; c) M. Lluncll, D. Casanova, J. Circra, J. M. Bofill, P. Alcmany, S. Alvarez, M. Pinsky, D. Avnir, SHAPE, version 2.1, University of Barcelona, Barcelona, Spain, and Hebrew University of Jerusalem, Jerusalem, Israel, 2005.
11. See, for example: a) F. Gao, L. Wang, G.-Z. Zhu, Y.-H. Liu, H. Yang, X. Li, K. Yang, *Dalton Trans*. **2019**, *48*, 13360; b) F. Gao, Y.-Q. Zhang, W. Sun, H. Liu, X. Chen, *Dalton Trans*. **2018**, *47*, 11696; c) X. Mei, X. Wang, J. Wang, Y. Ma, L. Li, D. Liao, *New J. Chem*. **2013**, 37, 3626; d) N. M. Randell, M. U. Anwar, L. N. Dawe, L. K. Thompson, *Inorg. Chem*. **2013**, *52*, 6731.
12. See, for example: a) J.-P. Sutter, M. L. Kahn, S. Golhen, L. Ouahab, O. Kahn, *Chem.-Eur. J*. **1998**, *4*, 571; b) L. Xi, H. Li, J. Sun, Y. Ma, J. Tang, L. Li, *Inorg. Chem.* **2020**, *59*, 443; c) J. Sun, Z. Sun, L. Li, J.-P. Sutter, *Inorg. Chem*. **2018**, *57*, 7507; d) J. Song, P. Hu, L.-J. Zhang, Z.-Y. Liu, J. Yu, R.-J. Xie, L.-Z. Huang, Y.-Y. Gao, *Inorg. Chem. Commun*. **2019**, *105*, 188; e) M. Zhu, Y. Li, L. Jia, L. Zhang, W. Zhang, *RSC Adv*. **2017**, *7*, 36895; f) J.-X. Xu, Y. Ma, G.-F. Xu, C. Wang, D.-Z. Liao, Z.-H. Jiang, S.-P. Yan, L.-C. Li, *Inorg. Chem. Commun.* **2008**, *11*, 1356;

g) H. Miao, H.-Q. Li, F.-X. Shen, H.-Y. Wei, B.-L. Wang, X.-Y. Wang, *Dalton Trans.* **2019**, *48*, 10337; h) L. Xi, J. Han, X. Huang, L. Li, *Magnetochemistry* **2020**, *6*, 48.

13. T. Gupta, T. Rajashkumar, G. Rajaraman, *Phys. Chem. Chem. Phys*. **2014**, *16*, 14568.

14. F. Luis, P. J. Alonso, O. Roubeau, V. Velasco, D. Zueco, D. Aguilà, J. I. Martínez, L. A. Barrios, G. Aromí, Communications Chemistry **2020**, *3*, 176.

15. A. Schweiger and G. Jeschke, Principle of pulse electron paramagnetic resonance, Oxford Univ. press, 2011.

16. R. Sayre, *J. Am. Chem. Soc.*, **1955**, *77*, 6689.

17. a) R.-G. Xie, Z.-J. Zhang, J.-M. Yan, D.-Q. Yuan, *Synth. Commun.* **1994**, *24*, 53; b) S. Serra, A. Alouane, T. Le Saux, S. Huvelle, R. Plasson, F. Schmidt, L. Jullien, R. Labruère, *Chem. Commun.* **2018**, *54*, 6396.

18. K. Bernot, L. Bogani, A. Caneschi, D. Gatteschi, R. Sessoli, *J. Am. Chem. Soc.*, **2006**, *128*, 7947.

19. a) C. A. Spinu, C. Pichon, G. Ionita, T. Mocanu, S. Calancea, M. Raduca, J. P. Sutter, M. Hillebrand, M. Andruh, *J. Coord. Chem.* **2021**, *74*, 279; b) S. Shimono, R. Tamura, N. Ikuma, T. Takimoto, N. Kawame, O. Tamada, N. Sakai, H. Matsuura, J. Yamauchi, *J. Org. Chem.* **2004**, *69*, 475.

20. S. Calancea, L. Carrella, T. Mocanu, V. Sadohin, M. Raduca, I. Gutu, J. C. da Rocha, M. G. F. Vaz, E. Rentschler, M. Andruh, *Eur. J. Inorg. Chem.* **2021**, *2021*, 567.

21. S. Stoll, A. Schweiger, *J. Magn. Reson.*, **2006**, *178*, 42–55.

22. K. Bader, D. Dengler, S. Lenz, B. Endeward, S.-D. Jiang, P. Neugebauer, J. van Slageren, *Nat. Commun.*, **2014**, *5*, 5304.

23. M.J. Frisch, G.W. Trucks, H.B. Schlegel, G.E. Scuseria, M.A. Robb, J.R. Cheeseman, G. Scalmani, V. Barone, B. Mennucci, G.A. Petersson, H. Nakatsuji, M. Caricato, X. Li, H.P. Hratchian, A.F. Izmaylov, J. Bloino, G. Zheng, J.L. Sonnenberg, M. Hada, M. Ehara, K. Toyota, R. Fukuda, J. Hasegawa, M. Ishida, T. Nakajima, Y. Honda, O. Kitao, H. Nakai, T. Vreven, J. A. Montgomery, J.E. Peralta, F. Ogliaro, M. Bearpark, J. J. Heyd, E. Brothers, K.N. Kudin, V.N. Staroverov, R. Kobayashi, J. Normand, K. Raghavachari, A. Rendell, J.C. Burant, S.S. Iyengar, J. Tomasi, M. Cossi, N. Rega, J. M. Millam, M. Klene, J.E. Knox, J.B. Cross, V. Bakken, C. Adamo, J. Jaramillo, R. Gomperts, R.E. Stratmann, O. Yazyev, A.J. Austin, R. Cammi, C. Pomelli, J.W. Ochterski, R.L. Martin, K. Morokuma, V.G. Zakrzewski, G.A. Voth, P. Salvador, J.J. Dannenberg, S. Dapprich, A.D. Daniels, O. Farkas, J.B. Foresman, J.V. Ortiz, J. Cioslowski, D.J. Fox, *GAUSSIAN 09, Revision C.01, Gaussian, Inc.*, *Wallingford CT* (2009).

24. A.D. Becke, *J. Chem. Phys*., **1993**, 98, 5648.

25. F. Weigend, R. Ahlrichs, *Phys. Chem. Chem. Phys.*, **2005**, 7, 3297.

Electronic Supporting Information

Synthesis of $[Tb_2(A\text{-}H)_2(hfac)_4]$ (5)

Compound $[Tb_2(A\text{-}H)_2(hfac)_4]$ has been synthesized using the following procedure. $[Tb(hfac)_3(H_2O)_2]$ (0.0625 mmol, 0.0510 g) was dissolved in 15 mL boiling *n*-heptane, then a solution of **A** (0.0625 mmol, 0.0104 g) in 3 mL $CHCl_3$ was added followed by a drop of triethylamine. The mixture was stirred for another minute and then it was let to cool down. Yellow crystals appeared after 1-2 days.

Synthesis of $(Et_3NH)[Tb(hfac)_4]$ (6)

Compound $(Et_3NH)[Tb(hfac)_4]$ has been synthesized using the following procedure. Over a hot solution of n-heptane (15 mL) containing $[Tb(hfac)_3(H_2O)_2]$, (0.04 mmol, 0.0326 g) two drops of triethylamine and 3 mL $CHCl_3$ were added. The mixture was stirred for another minute and then it was let to cool down. White crystals appeared after 1-2 days.

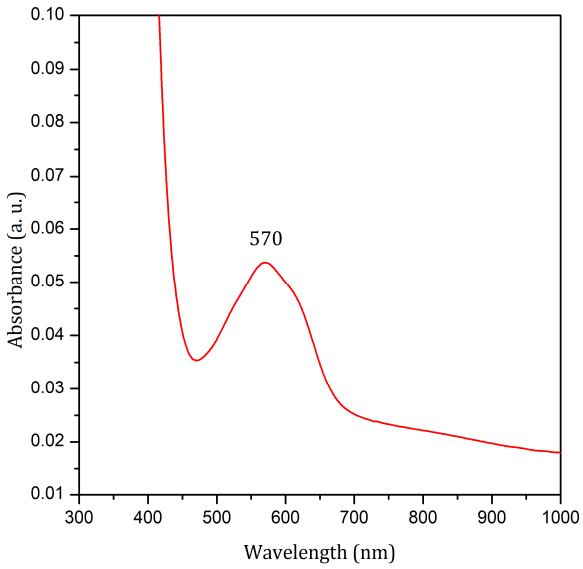

Figure S1. UV-VIS spectrum of the methanolic solution of (**B** + **C**).

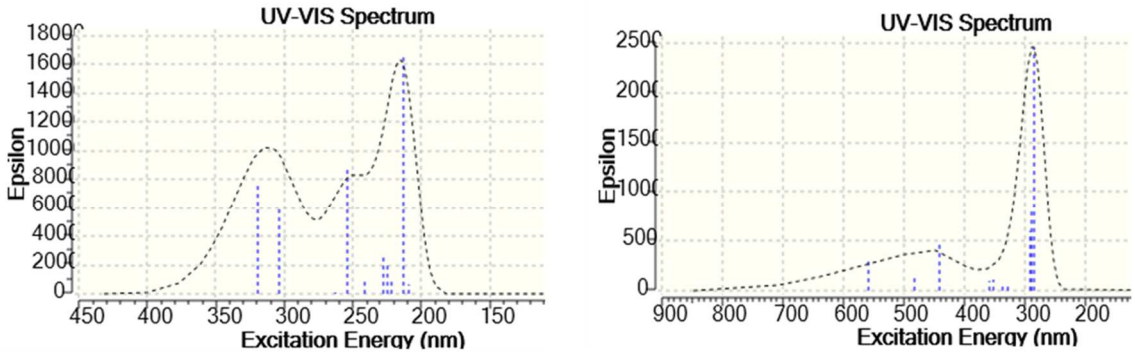

Figure S2. The calculated electronic spectra of **B** and **C,** optimized in methanol.

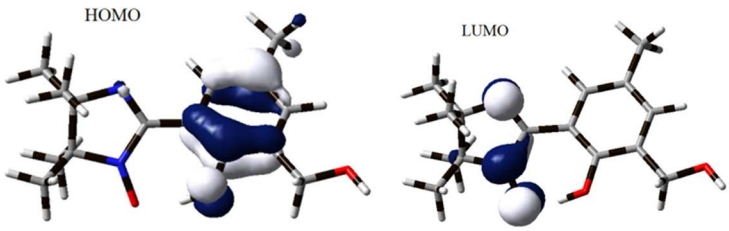

Figure S3. Frontier β molecular orbitals implied in the longest wavelength transition of **C** (560 nm).

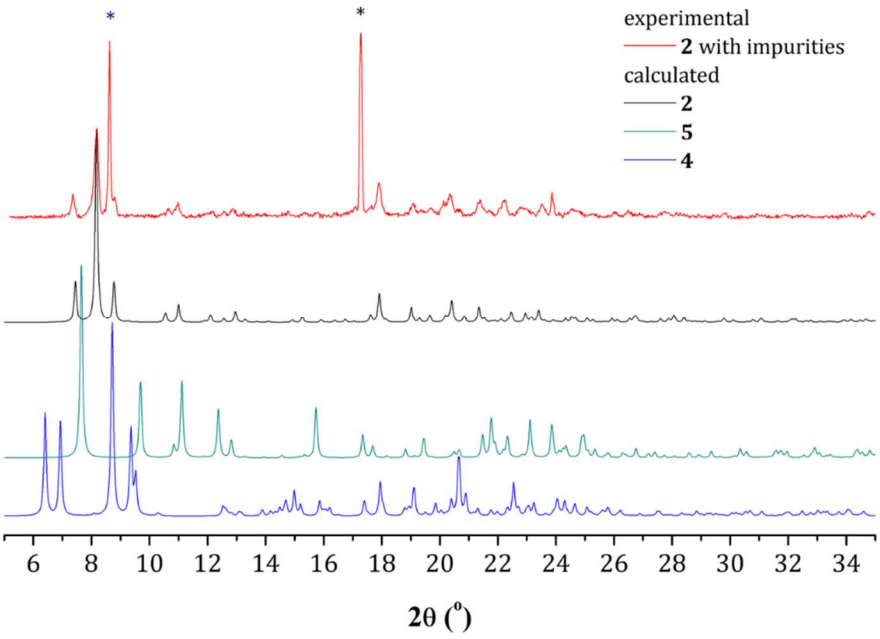

Figure S4. Experimental and simulated powder X-ray diffractograms of **2** versus simulated diffractograms of byproducts **4** and **5**. The picks attributed to the impurities in the experimental diffractogram are marked by star (*).

Table S1. Crystallographic data, details of data collection and structure refinement parameters for **B (1-9). B1**-**B4** are structures from different crystals from the same synthesis, while **B5-B9** are structures from different crystals from another synthesis.

Compound	**B1**	**B2**	**B3**	**B4**	**B5**
Chemical formula	$C_{15}H_{22}N_2O_4$	$C_{15}H_{22}N_2O_4$	$C_{15}H_{22}N_2O_4$	$C_{15}H_{22}N_2O_4$	$C_{15}H_{22}N_2O_4$
M (g mol^{-1})	294.35	294.35	294.35	294.35	294.35
Temperature, (K)	293(2)	293(2)	293(2)	293(2)	293(2)
Wavelength, (Å)	0.71073	0.71073	0.71073	0.71073	0.71073
Crystal system	*Orthorhombic*	*Orthorhombic*	*Orthorhombic*	*Orthorhombic*	*Orthorhombic*
Space group	$P2_12_12_1$	$P2_12_12_1$	$P2_12_12_1$	$P2_12_12_1$	$P2_12_12_1$
a (Å)	10.7450(7)	10.8219(6)	10.8216(5)	10.8276(7)	10.8356(11)
b (Å)	11.6104(8)	11.6911(6)	11.6844(5)	11.6951(6)	11.6868(9)
c (Å)	12.4249(7)	12.5013(6)	12.5029(7)	12.4817(9)	12.5165(10)
α (º)	90	90	90	90	90
β (º)	90	90	90	90	90
γ (º)	90	90	90	90	90
V (Å^3)	1550.04(17)	1581.66(14)	1580.92(13)	1580.56(18)	1585.0(2)
Z	4	4	4	4	4
D_c (g cm^{-3})	1.247	1.222	1.220	1.218	1.226
μ (mm^{-1})	0.090	0.088	0.088	0.088	0.089
F(000)	625	625	624	622	628
Goodness-of-fit on F^2	1.059	1.049	1.073	1.051	1.038
Final R_1, wR_2 [I>2σ(I)]	0.0452, 0.1139	0.0408, 0.1126	0.0405, 0.1133	0.0481, 0.1348	0.0442, 0.1128
R_1, wR_2 (all data)	0.0495, 0.1172	0.0465, 0.1163	0.0463, 0.1170	0.0589, 0.1424	0.0559, 0.1185
Largest difference peak and hole (e Å^{-3})	0.192, -0.213	0.208, -0.144	0.207, -0.145	0.292, -0.190	0.163, -0.146
Occupancy O4	0.80	0.80	0.77	0.73	0.90

Table S1. *(Continuation)*

Compound	**B6**	**B7**	**B8**	**B9**
Chemical formula	$C_{15}H_{22}N_2O_4$	$C_{15}H_{22}N_2O_4$	$C_{15}H_{22}N_2O_4$	$C_{15}H_{22}N_2O_4$
M (g mol^{-1})	294.35	294.35	294.35	294.35
Temperature, (K)	293(2)	293(2)	293(2)	293(2)
Wavelength, (Å)	0.71073	0.71073	0.71073	0.71073
Crystal system	*Orthorhombic*	*Orthorhombic*	*Orthorhombic*	*Orthorhombic*
Space group	$P2_12_12_1$	$P2_12_12_1$	$P2_12_12_1$	$P2_12_12_1$
a (Å)	10.8432(8)	10.8347(6)	10.8442(5)	10.8472(8)
b (Å)	11.6796(8)	11.6807(5)	11.6808(6)	11.6905(8)
c (Å)	12.4993(11)	12.5097(6)	12.5130(7)	12.5055(14)
α (º)	90	90	90	90
β (º)	90	90	90	90
γ (º)	90	90	90	90
V (Å^3)	1583.0(2)	1583.19(13)	1585.01(14)	1585.8(2)
Z	4	4	4	4
D_c (g cm^{-3})	1.231	1.228	1.226	1.226
μ (mm^{-1})	0.089	0.089	0.089	0.089
F(000)	630	629	628	629
Goodness-of-fit on F^2	1.093	1.070	1.065	1.061
Final R_1, wR_2 [I>2σ(I)]	0.0390, 0.0992	0.0344, 0.0888	0.0339, 0.0904	0.0387, 0.1054
R_1, wR_2 (all data)	0.0480, 0.1029	0.0406, 0.0922	0.0388, 0.0932	0.0477, 0.1093
Largest difference peak and hole (e Å^{-3})	0.139, -0.169	0.171, -0.147	0.166, -0.119	0.157, -0.138
Occupancy O4	0.94	0.91	0.89	0.91

Table S2. Selected bond lengths [Å] and angles (°) for **B** (see atom numbering scheme below).

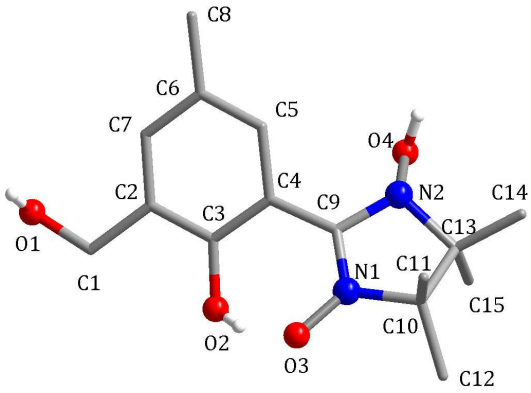

O1 – C1	1.406(3)
O2 – C3	1.348(3)
N1 – O3	1.343(3)
N1 – C9	1.304(3)
N2 – O4	1.412(3)
N2 – C9	1.381(3)
N1 – C9 – N2	109.54(19)
C9 – N1 – O3	125.66(19)
C9 – N2 – O4	113.66(17)
C9 – N1 – C10	111.63(18)
C9 – N2 – C13	107.03(18)

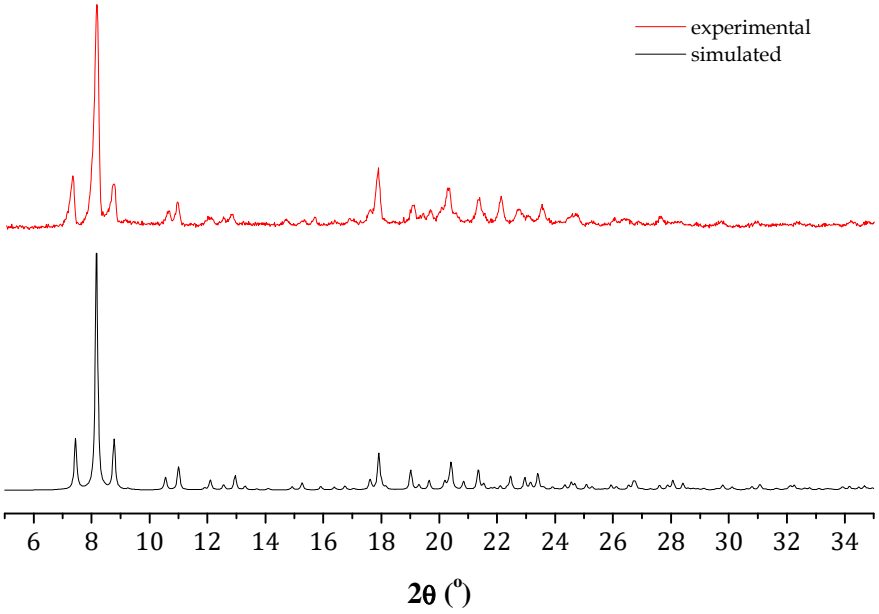

Figure S5.1. Measured (red) and calculated (black) powder X-ray diffraction patterns of **1**.

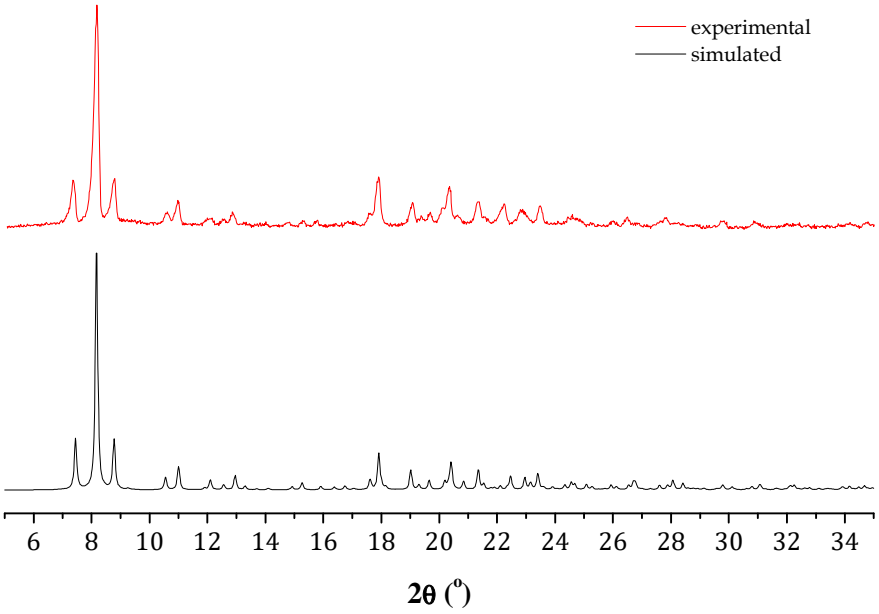

Figure S5.2. Measured (red) and calculated (black) powder X-ray diffraction patterns of **2**.

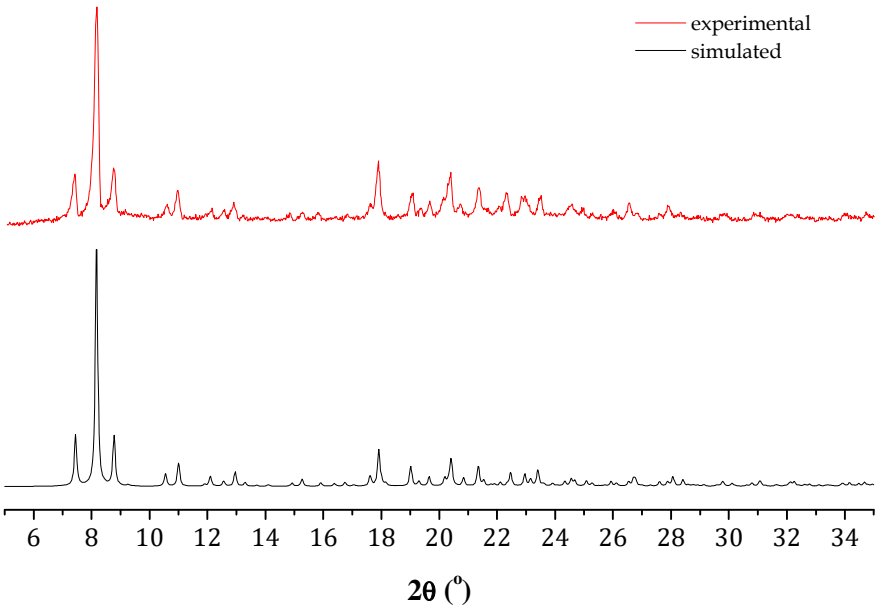

Figure S5.3. Measured (red) and calculated (black) powder X-ray diffraction patterns of **3**.

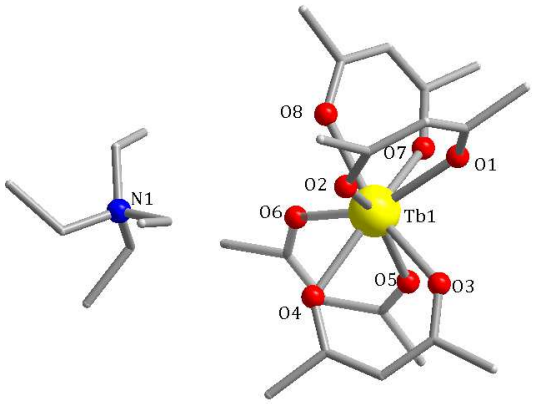

Figure S6. Perspective view of crystal structure of compound **6**. Hydrogen and fluorine atoms have been omitted for clarity. The three ethyl groups from triethyl ammonium cation are disordered on four crystallographic positions.

Table S3. SHAPE analysis for compounds **1-3** was performed for the coordination geometry of the Ln ions with respect to 13 reference polyhedra. All dinuclears being isostructural, crystallizing in *P* 1 $2_1/n$ space group the two metal ions are identical, and they have the same coordination environment, thus just one will be described. A perfect match between the environment of the Ln ions and the ideal polyhedron is indicated by zero value. Highlighted are the closest polyhedra for each case.

	1	**2**	**3**		
OP-8	31.865	31.406	31.235	D_{8h}	Octagon
HPY-8	22.525	22.834	22.967	C_{7v}	Heptagonal pyramid
HBPY-8	15.981	16.369	16.362	D_{6h}	Hexagonal bipyramid
CU-8	10.005	10.085	9.96	O_h	Cube
SAPR-8	**0.945**	**0.838**	**0.743**	D_{4d}	Square antiprism
TDD-8	2.072	2.086	2.157	D_{2d}	Triangular dodecahedron
JGBF-8	15.493	15.313	15.593	D_{2d}	Johnson gyrobifastigium J26
JETBPY-8	27.322	27.254	27.372	D_{3h}	Johnson elongated triangular bipyramid J14
JBTPR-8	2.877	2.936	2.914	C_{2v}	Biaugmented trigonal prism J50
BTPR-8	2.248	2.354	2.354	C_{2v}	Biaugmented trigonal prism
JSD-8	4.705	4.701	4.815	D_{2d}	Snub diphenoid J84
TT-8	10.694	10.781	10.664	T_d	Triakis tetrahedron
ETBPY-8	22.736	22.424	22.577	D_{3h}	Elongated trigonal bipyramid

Table S4. SHAPE analysis for compounds **4** and **5** was performed for the coordination geometry of the Tb ions with respect to 13 reference polyhedra. In the case of the dinuclear, which crystallizes in *P* 1 $2_1/n$ space group, the two metal ions are identical, and they have the same coordination environment, thus just one will be described. Highlighted are the closest polyhedra for each case.

	4	**5**		
OP-8	31.552	30.155	D_{8h}	Octagon
HPY-8	23.685	22.958	C_{7v}	Heptagonal pyramid
HBPY-8	13.314	16.193	D_{6h}	Hexagonal bipyramid
CU-8	5.975	10.739	O_h	Cube
SAPR-8	1.813	1.245	D_{4d}	Square antiprism
TDD-8	**0.530**	**1.017**	D_{2d}	Triangular dodecahedron
JGBF-8	15.946	13.373	D_{2d}	Johnson gyrobifastigium J26
JETBPY-8	28.118	28.659	D_{3h}	Johnson elongated triangular bipyramid J14
JBTPR-8	3.254	2.157	C_{2v}	Biaugmented trigonal prism J50
BTPR-8	2.652	1.585	C_{2v}	Biaugmented trigonal prism
JSD-8	3.803	3.393	D_{2d}	Snub diphenoid J84
TT-8	6.793	11.587	T_d	Triakis tetrahedron
ETBPY-8	24.548	23.572	D_{3h}	Elongated trigonal bipyramid

Table S5. Selected bond distances [Å] and angles (°) for compounds **1-3** (see atom numbering scheme below).

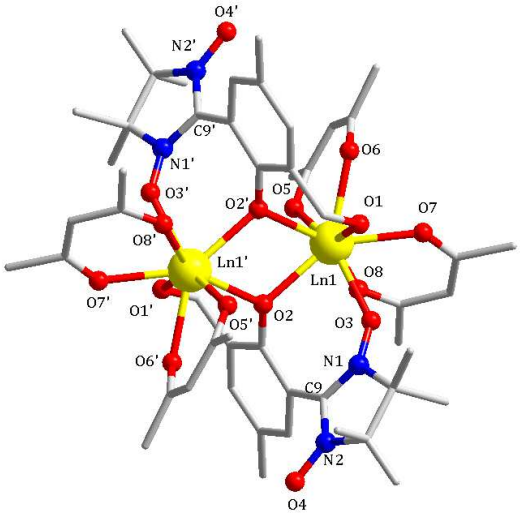

1		2		3	
Gd1···Gd1'	3.9412(11)	Tb1···Tb1'	3.9063(5)	Dy1···Dy1'	3.8603(9)
Gd1···O1	2.408(7)	Tb1···O1	2.407(4)	Dy1···O1	2.388(7)
Gd1···O2	2.364(6)	Tb1···O2	2.356(3)	Dy1···O2	2.340(5)
Gd1···O3	2.365(8)	Tb1···O3	2.343(4)	Dy1···O3	2.324(7)
Gd1···O5	2.374(8)	Tb1···O5	2.364(4)	Dy1···O5	2.353(8)
Gd1···O6	2.413(8)	Tb1···O6	2.364(4)	Dy1···O6	2.384(7)
Gd1···O7	2.357(9)	Tb1···O7	2.357(4)	Dy1···O7	2.341(7)
Gd1···O8	2.402(9)	Tb1···O8	2.382(4)	Dy1···O8	2.367(7)
N1···O3	1.270(11)	N1···O3	1.276(6)	N1···O3	1.261(10)
N2···O4	1.292(12)	N2···O4	1.284(6)	N2···O4	1.313(11)
Gd1-O2-Gd1'	112.3(2)	Tb1-O2-Tb1'	111.95(12)	Dy1-O2-Dy1'	111.7(2)
O3-N1-C9	127.9(10)	O3-N1-C9	127.3(5)	O3-N1-C9	126.7(9)
O4-N2-C9	123.6(10)	O4-N2-C9	124.6(5)	O4-N2-C9	124.5(10)

Table S6. Selected bond distances [Å] and angles (°) for compounds **4** and **5** (see atom numbering scheme below).

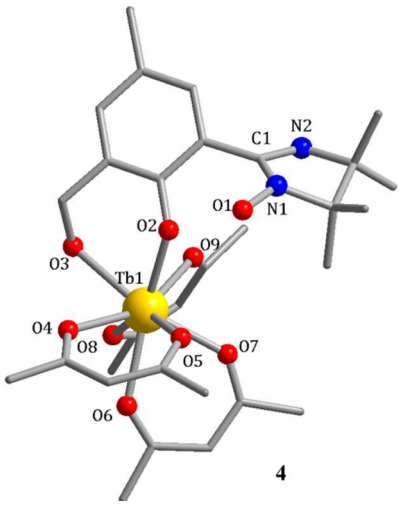

4

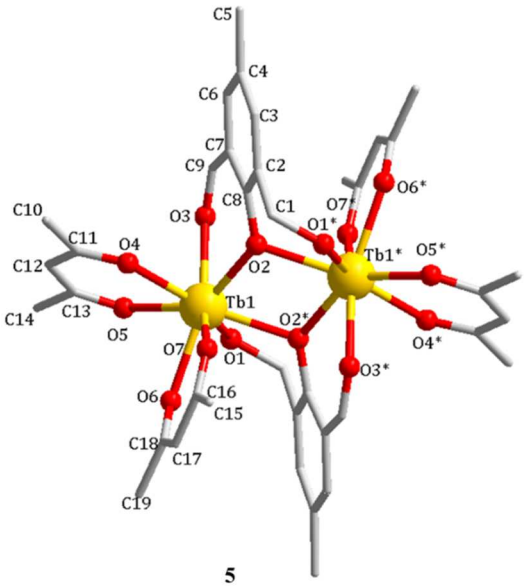

5

4		**5**	
Tb1···O2	2.297(5)	Tb1···O1	2.418(3)
Tb1···O3	2.410(5)	Tb1···O2	2.365(3)
Tb1···O4	2.417(5)	Tb1···O3	2.418(4)
Tb1···O5	2.348(5)	Tb1···O4	2.330(3)
Tb1···O6	2.384(5)	Tb1···O5	2.383(3)
Tb1···O7	2.343(5)	Tb1···O6	2.353(3)
Tb1···O8	2.343(5)	Tb1···O7	2.395(3)
Tb1···O9	2.380(5)	Tb1-O2-Tb1*	110.27(12)
N1···O1	1.387(8)		
O1-N1-C1	124.3(5)		
N1-C1-N2	110.0(6)		

Table S7. Data collection and refinement parameters for compounds **4-6.**

Compound	**4**	**5**	**6**
Chemical formula	$C_{30}H_{24}F_{18}N_2O_9Tb$	$C_{38}H_{22}F_{24}O_{14}Tb_2$	$C_{26}H_{20}F_{24}NO_8Tb$
M (g mol^{-1})	1057.43	1476.39	1089.35
Temperature, (K)	293(2)	293(2)	293(2)
Wavelength, (Å)	0.71073	0.71073	0.71073
Crystal system	*Monoclinic*	*Monoclinic*	*Monoclinic*
Space group	*C2/c*	*P21/n*	*P21/n*
a (Å)	25.4964(18)	8.9394(2)	12.0268(4)
b (Å)	12.0971(8)	18.2439(6)	16.5294(5)
c (Å)	27.5847(16)	15.0784(5)	21.0265(7)
α (º)	90	90	90
β (º)	90.998(6)	98.580(3)	101.220(3)
γ (º)	90	90	90
V (Å^3)	8506.7(10)	2431.60(13)	4100.1(2)
Z	8	2	4
D_c (g cm^{-3})	1.651	2.016	1.765
μ (mm^{-1})	1.789	3.038	1.876
F(000)	4136	1416	2112
Goodness-of-fit on F^2	1.041	1.034	1.030
Final R_1, wR_2 [I>2σ(I)]	0.0589, 0.1453	0.0354, 0.0846	0.0537, 0.1568
R_1, wR_2 (all data)	0.0831, 0.1570	0.0420, 0.0882	0.0634, 0.1693
Largest difference peak and hole (e Å^{-3})	1.030, -0.551	1.015, -0.456	1.041, -0.747

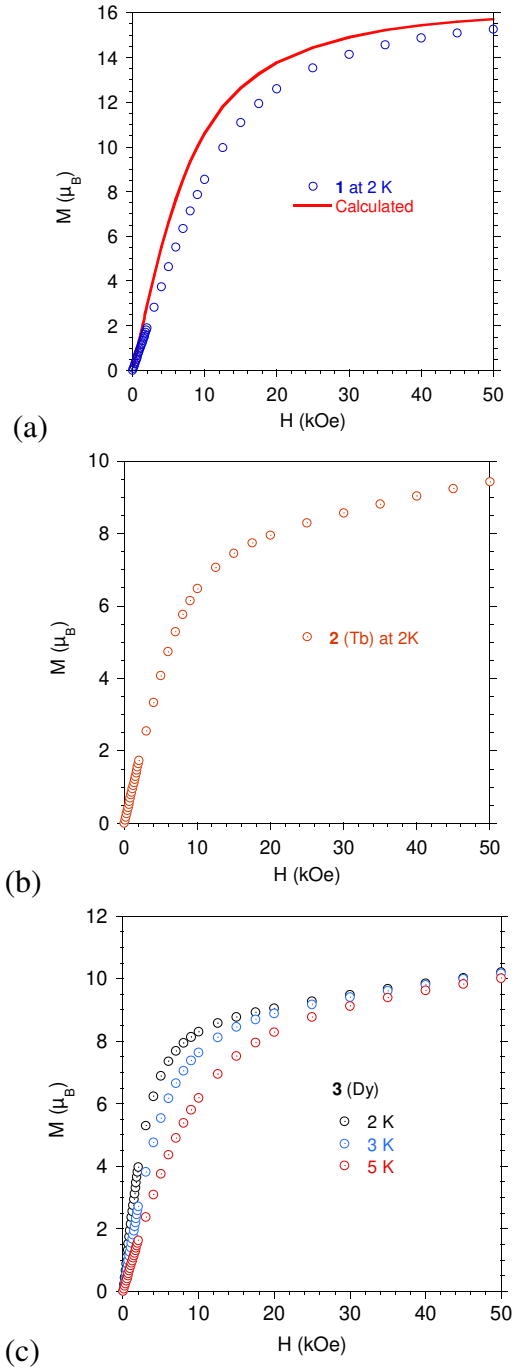

Figure S7. Field dependence of the magnetization for (top-down) **1** (Gd), **2** (Tb), and **3** (Dy). Red full line is the magnetization calculated with Brillouin functions for two Gd and two radical moieties at 2 K without exchange interactions.

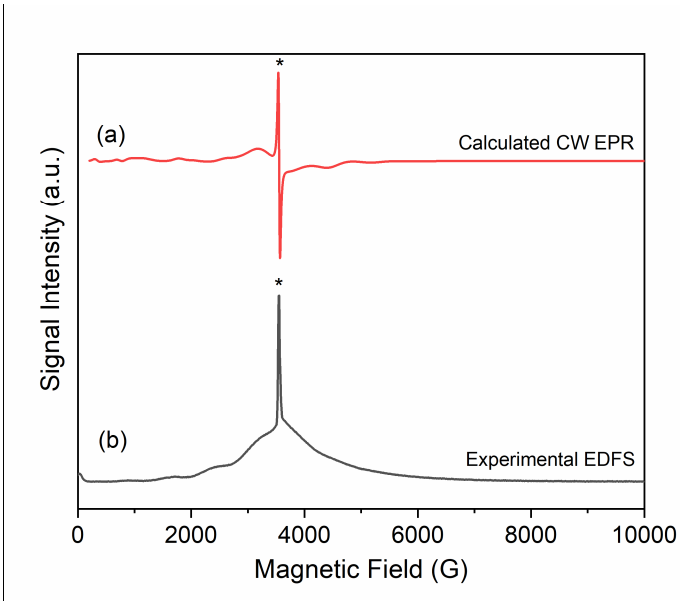

Figure S8. (a) Calculated EPR spectrum of **1** using the same parameters from powder data (g = 1.996, D = 0.04 cm^{-1}, E = 0.013 cm^{-1}). (b) Experimental EDFS spectrum of **1** at 6 K. The central line marked with (*) is assigned to the nitronyl nitroxide radicals in **1**.

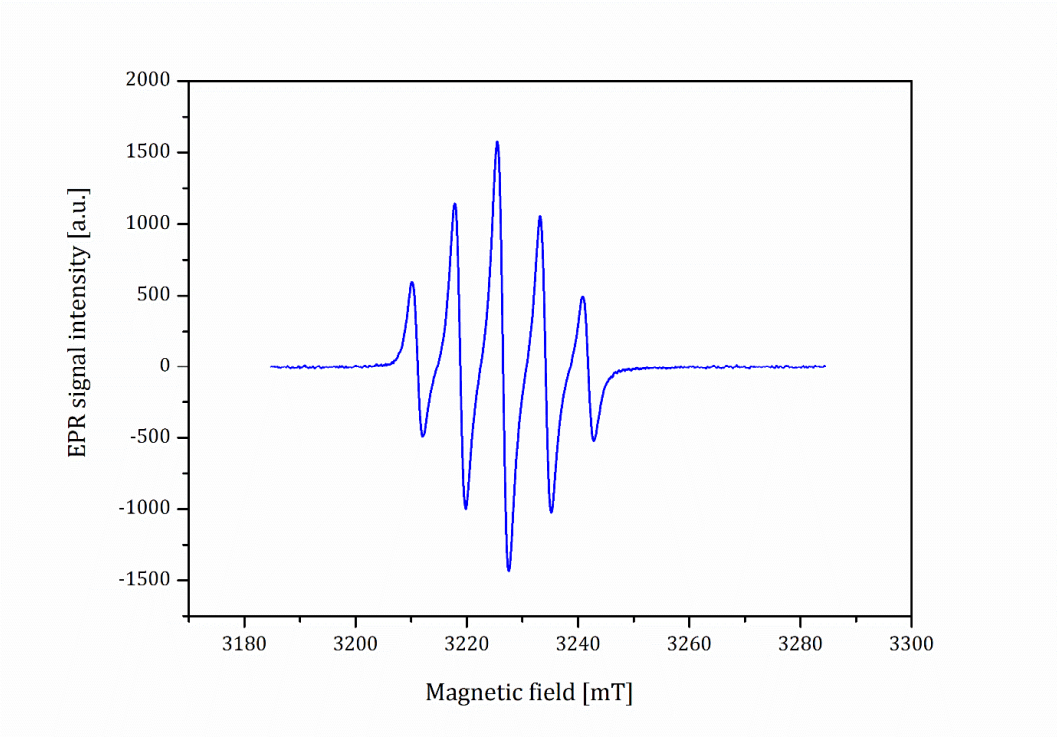

Figure S9. EPR spectrum of H_2L in CH_2Cl_2. The hyperfine constant a_N = 7.65 G.